Prediction of interfacial fracture between concrete and fiber reinforced polymer (FRP) by using cohesive zone modeling

Kyoungsoo Park [a], Kyungsu Ha [a], Habeun Choi [a], Changjoon Lee [b],*

[a] Department of Civil & Environmental Engineering, Yonsei University, 50 Yonsei-ro Seodaemun-gu, Seoul, 120-749, Republic of Korea
[b] Department of Architectural Engineering, Chungbuk National University, 52 Naesudong-ro Heungdeok-gu Chungju, Chungbuk, 361-763, Republic of Korea

ARTICLE INFO

ABSTRACT

Interfacial debonding between concrete and fiber reinforced polymer (FRP) is investigated through integrating experiments and computations. An experimental program is designed to evaluate interfacial fracture parameters of mode-I through cutting and bonding specimens with an FRP sheet. The evaluated fracture parameters, i.e. the fracture energy and the bonding strength, are confirmed by predicting FRP debonding failure with the cohesive zone modeling approach. In the cohesive zone model, a traction-separation relation for FRP debonding is proposed with a shape index while providing various initial descending slopes. Computational results of the cohesive zone model agree well with three-point bending test results for both FRP debonding and plain concrete fracture. Furthermore, both experimental and computational results demonstrate that the fracture energy and the cohesive strength are essential fracture parameters for the prediction of FRP debonding behavior.

1. Introduction

Fiber reinforced polymer (FRP) has been widely utilized in order to strengthen and retrofit concrete structures because of high strength-to-weight ratio, corrosion resistances, low cost for retrofitting, etc. [8,18,27,45]. Thus, recent design codes provide guidelines for strengthening concrete structures with FRP [2,15]. For sustainable FRP strengthened structures, one of the fundamental aspects is to understand and predict delamination failure mechanisms between concrete and FRP.

Failure behavior of FRP strengthened structures have been investigated through developing various experimental testing configurations [45]. For the investigation of shear anchorage failure of an FRP plate, named as plate end debonding, single shear tests and pull tests were generally utilized through varying bond length, sizes and material properties of FRP and concrete [44,50]. Because the asymmetrical configuration of a single shear test can lead to difficulties in controlling progressive FRP debonding [25], double shear tests were employed, which resulted in a symmetry configuration [7,39]. In addition, FRP-concrete interfacial fracture initiated from an intermediate flexural or flexural-shear crack on RC beams, named as intermediate crack-induced debonding, was also investigated, especially for slender members and/or members with a relatively thin FRP plate [38,46].

Based on FRP debonding test results, various bond strength models [9,20,40] and analytical bond-slip models [23,26] were developed to predict the FRP-concrete bond strength and failure load in conjunction with the concrete strength, FRP plate stiffness, effective bond length, load-slip curves, etc. For example, Smith and Teng [41] assessed existing bond strength models through comparing model predictions with test results of FRP-strengthened simply supported RC beams. Lu et al. [23] also reviewed existing analytical models for bond behavior, and compared the predicted bond strength with pull test results. However, because such analytical models are based on empirical parameter calibrations and the linear elastic theory, they are limited to describe nonlinear progressive delamination process.

To represents nonlinear debonding of the FRP-concrete interface, several computational methods were utilized, which include bond elements [47], plastic-damage models [11,32], and cohesive zone models [10,34,48]. A simple bond element was employed in conjunction with the modified compression field theory for investigating behavior of RC members with externally bonded FRP [47]. Pesic and Pilakoutas [32] described FRP debonding through

* Corresponding author.
E-mail addresses: k-park@yonsei.ac.kr (K. Park), tnrudgk@gmail.com (K. Ha), bluegean@yonsei.ac.kr (H. Choi), cjlee@cbnu.ac.kr (C. Lee).

defining epoxy adhesive as an ideal isotropic elasto-plastic material. Coronado and Lopez [11] employed a plastic-damage model of concrete [24] to represent a crack band due to debonding and plain concrete damage on RC beams. Note that the failure of an FRP-concrete interface was smeared in a crack band of a fixed width.

Alternatively, nonlinear FRP debonding process was represented by employing the concept of the conehsive zone model, which is the choice of the present study. The cohesive zone model approximates progressive nonlinear fracture process zone [3,12], and is extensively utilized for fracture of various composite materials such as plain concrete [13,17,37], fiber reinforced concrete [30], asphalt concrete [21,42], etc. For debonding of the FRP-concrete interface, Wu and Yin [48] employed the cohesive crack model to investigate interactions among fracture parameters such as the interfacial fracture energy, the bond strength, the fracture energy of concrete, and the tensile strength of concrete. Coronado and Lopez [10] performed sensitivity analysis of RC beams strengthened with FRP laminates, and emphasized that the fracture energy of the interface was needed to accurately predict plate-debonding failures of strengthened RC beams.

For the use of the cohesive zone model, it is essential to define the relationship between cohesive traction and separation in conjunction with fracture parameters. Fracture parameters include, for example, the fracture energy, the cohesive strength, and the shape of the traction–separation relationship. Then, Qiao and Xu [35] estimated the mode-I fracture energy of an FRP-concrete interface by utilizing the work-of-fracture method [16] with a three-point bending test. However, few test configurations exist for the approximation of the cohesive strength. Note that Qiao and Chen [34] employed a beam theory and critical load to calculate the cohesive strength, which resulted in a wide range of the interfacial strength (i.e. 3 MPa ~ 10 MPa). Thus, their computational results provided overestimation on the post-peak load behavior while displaying a wide range of the peak load. For the shape of a traction-separation relation of FRP debonding, a linear softening model was generally used [22,34,48], which can lead to the overestimation of load carrying capacity [14]. Furthermore, no test method has been reported for the direct measurement of the fracture energy and the cohesive strength in mode-II because of difficulties in capturing the post-peak load for the FRP-concrete debonding. Therefore, an experimental program is necessary, which consistently provides fracture parameters such as the fracture energy and the cohesive strength for the interfacial fracture between concrete and FRP.

In the present paper, the mode-I interfacial fracture between concrete and FRP is investigated through integrating fracture tests and computational simulation. An experimental program is designed to estimate fracture parameters which include both the fracture energy and the cohesive strength. The evaluated fracture parameters are validated through predicting interfacial fracture behavior between concrete and FRP. Additionally, a traction-separation relation for FRP debonding is proposed in this study to provide various descending slopes with a shape index. The remainder of the paper is organized as follows. An experimental program and test results are presented in Section 2. Based on the test results, fracture parameters are estimated in Section 3. Section 4 proposes a traction-separation relation for FRP debonding, and briefly describes the cohesive zone model for plain concrete. In Section 5, a computational framework and its results are provided. Finally, the key finding of the present work is summarized in Section 6.

2. Design of experimental program

In order to estimate fracture parameters for the interfacial

Table 1
Mix proportions of concrete.

	Water	Cement	Coarse aggregate	Fine aggregate
Specific gravity	1.0	3.15	2.64	2.49
Unit weight (kg/m^3)	199	362	833	876

fracture between concrete and FRP, an experimental program is designed including three-point bending tests, splitting tests and compressive strength tests. A three-point bending test is employed to evaluate the fracture energy while a splitting test configuration is proposed to approximate the bond strength. A compressive strength test of concrete is performed to estimate the elastic modulus of concrete. For such tests, three test sets are prepared, i.e. FRP debonding set 1 (FRP-1 set), FRP debonding set 2 (FRP-2 set), and plain concrete set (PC set). Three specimens are prepared for each test set. The details of materials, specimen preparations, test procedures and results are described in the following subsections.

2.1. Materials

Normal strength concrete was prepared for the experimental program. Table 1 shows mix proportions of a concrete material. The water to cement ratio was 0.55, and the fine to coarse aggregates ratio was approximately 0.5. ASTM type I cement, crushed stone with a maximum size of 20 mm, and river sand were used for the binder, coarse aggregates, and fine aggregates, respectively.

FRP was fabricated with glass fiber sheets, epoxy resin and hardener, which were obtained from Conclinic Co. Ltd. in Republic of Korea. Epoxy resin is mixed with hardener in the ratio of 4:1 by weight, and then glass fiber sheets were submerged in the epoxy resin/hardener mixture. Material properties of FRP and glass fiber sheets were given by Conclinic Co. Ltd. The tensile strength and the elastic modulus of FRP were 5000 MPa and 250 GPa, respectively, and the tensile strain at failure was approximately 0.02 ~ 0.03. The unit weight of a glass fiber sheet was 950 g/cm^2 and its tensile strength was 700 MPa.

2.2. Specimen preparation

Three types of test specimens were fabricated, i.e. prismatic beam specimens for a three-point bending test, cylinder specimens for a splitting test and prism specimens for a compressive strength test. For each test, FRP-1, FRP-2 and PC sets were prepared. Note that each test set was fabricated at the same day while the concrete materials used for these tests were produced in different batches due to limited laboratory conditions.

2.2.1. Prismatic beam specimen for a three-point bending test

Prismatic beam specimens with dimensions of 80 × 150 × 700 mm were cast for a three-point bending test. The beam specimens were de-molded at the age of one day and cured in water for 27 days. For the PC set, an initial notch of 50 mm was created by using a saw cut machine. For the FRP-1 and FRP-2 sets, the geometry of test specimens is described in Fig. 1(a). The cast specimens were cut in half, and the epoxy resin/hardener mixture was applied on both cut surfaces. A glass fiber sheet (80 × 150 mm) was submerged in the epoxy resin/hardener mixture for 2 min, and then placed on the cut surface of one half-beam. In order to create an initial notch of 50 mm along the interface between FRP and concrete, two vinyl sheets (80 × 50 mm) were placed on top of the glass fiber sheet, i.e. no bonding between the two vinyl sheets. Finally, the other half-beam was placed on the one half-beam so as to complete the fabrication of the FRP beam specimens. The FRP
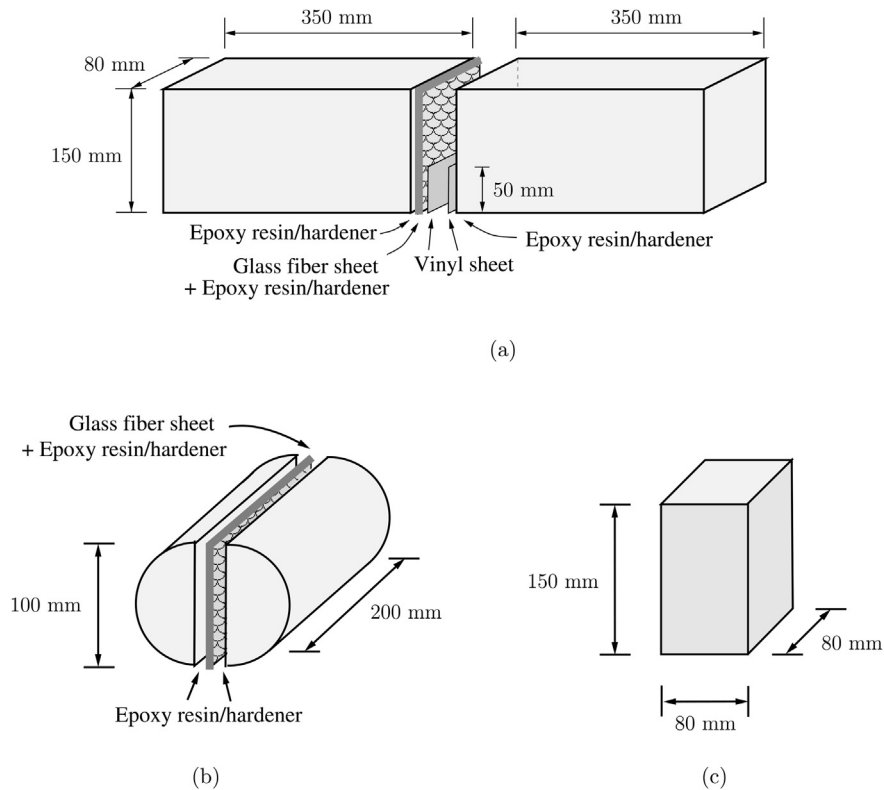
Fig. 1. Geometry of test specimens: (a) Three-point bending test for FRP debonding test sets, (b) splitting test for FRP debonding test sets, and (c) compressive strength test of plain concrete.

specimens were stored in laboratory condition for 14 days to cure the epoxy resin.

2.2.2. Cylinder specimen for a splitting test

Cylinder specimens with dimension of 100 mm diameter by 200 mm length were cast for a splitting test of FRP debonding and plain concrete. Cylinder specimens were de-molded at the age of one day and cured in water for 27 days. For each FRP debonding set, three cylinder specimens were cut in half along the longitudinal direction, as shown in Fig. 1(b). The epoxy resin/hardener mixture was applied on both cut surfaces of a cylinder, and a glass fiber sheet (100 mm by 200 mm) was submerged in the epoxy resin/hardener mixture for 2 min. The submerged glass fiber sheet was placed in between two cut half-cylinders, which completes the fabrication of the FRP cylinder specimen (Fig. 1(b)). The FRP specimens were stored in laboratory condition for 14 days to cure the epoxy resin.

2.2.3. Prism specimen for a compressive strength test

For compressive strength tests, prism specimens were prepared with the area of 80 × 80 mm and the height of 150 mm (Fig. 1(c)). Three prism specimens for each test set were directly obtained from the corresponding beam specimens. After the completion of three-point bending tests, beam specimens were cut in a length of 80 mm by using a saw cut machine, which results in the prism specimens.

2.3. Test procedure and result

Three-point bending tests, splitting tests and compressive strength tests were performed. From a three-point bending test, crack mouth opening displacement (CMOD) versus load relations were measured to estimate the fracture energy. The tensile strength and the compressive strength were evaluated from splitting and compressive strength tests, respectively.

2.3.1. Three-point bending test

An experimental setup for a three-point bending test is described in Fig. 2. In order to measure CMOD, a crack opening displacement (COD) gauge was installed to a specimen with the help of knife edges attached near the crack mouth. The edge-to-edge space between the knife edges was 10 mm and the thickness of the knife edges was 6 mm. All bending specimens were tested using an MTS closed-loop testing machine under the constant COD rate of 0.05 mm/min. Load and COD response data were collected using a data acquisition system. Note that the change of the COD gauge response corresponds to CMOD.

Experimental results of the FRP debonding sets and the plain concrete set are illustrated in Figs. 3 and 4, respectively. In each figure, averaged test results are also included in a white circled line. For FRP debonding tests, the peak loads of three replicates were 3.58 kN ~ 3.88 kN for the FRP-1 set, and 4.48 kN ~ 5.13 kN for the FRP-2 set, which displays small deviation for each replicate but relatively large difference for each set. The difference for each test set may be because each test set was prepared in different batches and days. In addition, both elastic and post-peak load behavior demonstrate similar behavior for each replicate except one test result in the FRP-1 set (i.e. FRP1-1 in Fig. 3(a)). In the test of FRP1-1, interfacial fracture was not propagated from an initial notch, and thus provided a relatively higher post-peak load. Such behavior might be associated with the existence of relatively large initial defects within the concrete-FRP interface. Then, the FRP1-1 result was not considered for the fracture energy evaluation.
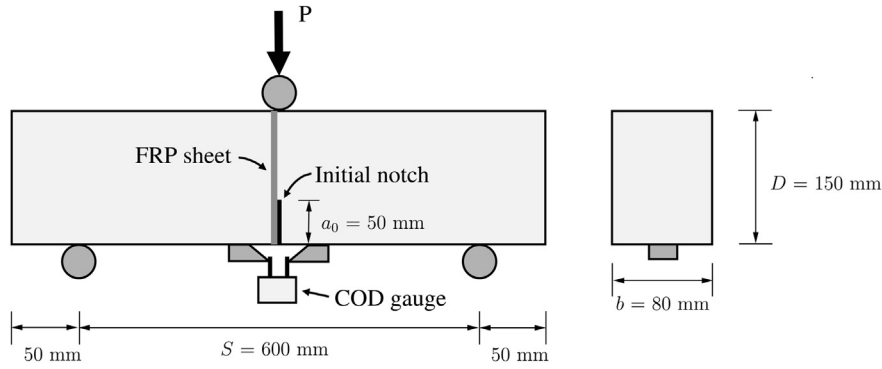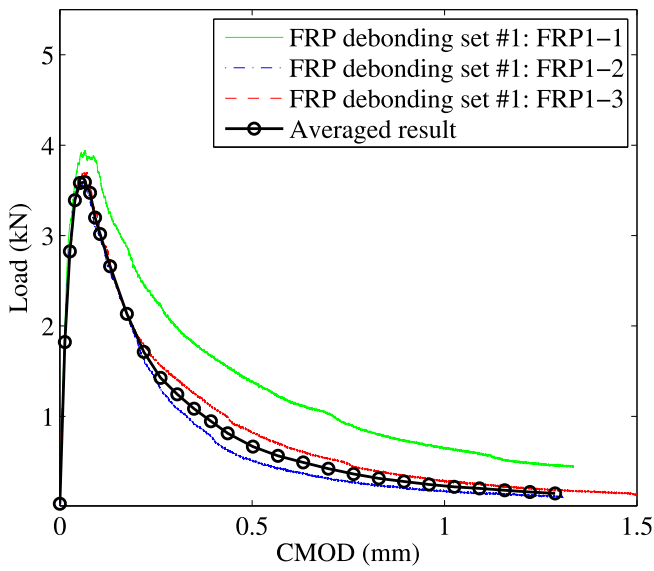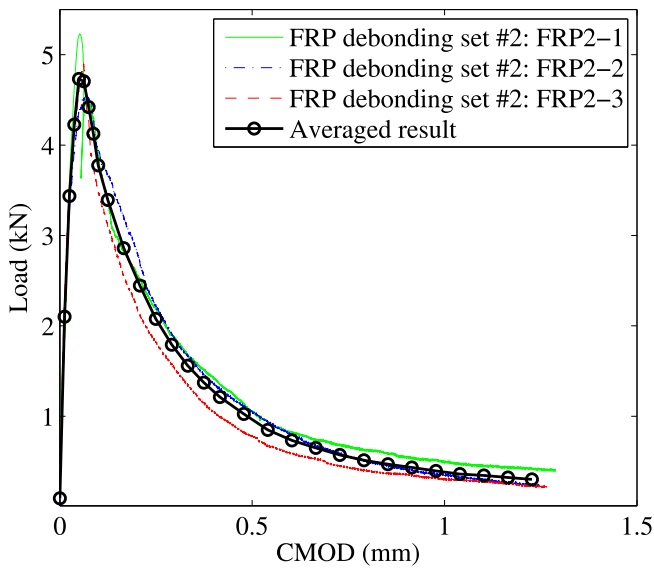
Fig. 2. Experimental setup for a three-point bending test.

(a)

Fig. 4. Three-point bending test results of plain concrete.

(b)

Fig. 3. Three-point bending test results for FRP debonding: (a) FRP-1 set and (b) FRP-2 set.

2.3.2. Splitting test

A splitting test was conducted using the cylinder specimens of the FRP debonding sets and the plain concrete set. The test was followed by the standard rule described in ASTM C 496. Note that an FRP sheet in the cylinder specimens was aligned to the load line so that "splitting" between an FRP sheet and concrete matrix could occur along the vertical direction, as shown in Fig. 5. In the experiment of the FRP sets, "splitting" failure was observed, as expected, along the either one of the two interfaces which exist between an FRP sheet and concrete. Table 2 summarizes the splitting test results. The average indirect tensile strength is obtained from three replicates for each test set.

2.3.3. Compressive strength test

A uniaxial compressive strength test was conducted using the prism specimens of the plain concrete set and the FRP debonding sets. Three replicates per each type of test set were used for this test. The uniaxial compressive strength of the three test sets is illustrated in Table 3. The averaged compressive strength of the FRP-1, FRP-2 and PC sets were 26.65 MPa, 30.61 MPa and 24.83 MPa, respectively. Based on the averaged compressive strength and the ACI building code (ACI 318), the elastic modulus was estimated, as shown in Table 3.
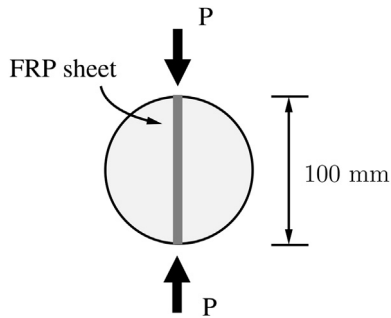
Fig. 5. Geometry of the splitting test for the FRP debonding sets.

Table 2
Splitting test results for each test set.

	Indirect tensile strength (MPa)			
	Specimen #1	Specimen #2	Specimen #3	Average
FRP debonding set 1	3.52	3.77	2.43	3.24
FRP debonding set 2	3.90	3.95	3.97	3.94
Plain concrete	2.48	3.19	2.46	2.71

3. Evaluation of fracture parameters

Based on the experimental program performed in the previous section, the fracture energy and the cohesive strength are evaluated. The fracture energy is obtained from the three-point bending test results in conjunction with the work-of-fracture method [16], while the cohesive strength is simply approximated by using the splitting test results.

3.1. Fracture energy

The fracture energy is obtained from the experimental load-CMOD curves on the basis of the work-of-fracture method [16]. The amount of work for the complete failure of a beam can be equivalent to the required energy for the creation of fracture area. Then, the total fracture energy (G_F) is calculated through dividing the total work by the fracture area, i.e.

$$G_F = \frac{W_0 + W_s}{b(D - a_0)} \tag{1}$$

where the total work consists of the work done by the applied load (W_0) and the work done by the self-weight (W_s). The work done by the applied load corresponds to the area under the load versus displacement curve, while the work done by the self-weight is approximated by $2P_0u_0$ [33]. Note that u_0 is displacement at the failure of a beam, and P_0 is defined as the central load that produces the same central bending moment as the system of self-weight, i.e. $P_0 = mg(2S - L)/2S$, where m and g are the mass of a beam and the acceleration of gravity, respectively. The calculated total fracture energy is summarized in Table 4 for each test set. Note that the total

Table 4
Calculated total fracture energy for each test set.

	Total fracture energy (N/m)			
	Specimen #1	Specimen #2	Specimen #3	Average
FRP debonding set 1	N/A	153.6	196.7	175
FRP debonding set 2	235.1	222.0	194.1	217
Plain concrete	259.5	225.2	267.7	251

fracture energy of plain concrete is higher than the interfacial fracture energy of the FRP debonding test sets.

3.2. Cohesive strength

The cohesive strength for the interface between concrete and FRP is simply approximated by employing the splitting test. Note that the cohesive strength of plain concrete was also calculated by using the splitting test [31,37] although the test may provide the influence of specimen geometry and the width of the load-bearing strip [36]. The averaged bonding strength for the FRP-1 and FRP-2 sets are 3.24 MPa and 3.94 MPa, respectively, as listed in Table 2. Additionally, the averaged splitting strength of plain concrete is 2.71 MPa, which is lower than the FRP bonding strength of both test sets.

3.3. Remarks

The experimental results of the splitting test demonstrate that the FRP bonding strength is higher than the tensile strength of plain concrete. Thus, one might expect that the bonding between FRP and concrete is strong enough to provide equivalent or higher load carrying capacity for FRP bonded specimens. However, the above expectation is not always true, as shown in Fig. 6. Fig. 6 demonstrates averaged load versus CMOD curves of the three-point bending test for each test set. The load carrying capacity of the FRP-1 set is lower than the capacity of the PC set, while the peak load of the FRP-2 set is higher than the peak load of plain concrete. In addition, the FRP-1 and FRP-2 sets displays lower post-peak load behavior than the plain concrete set. This is because the total fracture energy of FRP debonding is lower than the fracture energy of the plain concrete case (see Table 4). Note that the plain concrete dissipates more energy than the FRP debonding, because the PC set provides larger area under the load-CMOD curve than the FRP debonding sets. In conclusion, both the fracture energy and the cohesive strength should be considered for predicting interfacial fracture behavior between concrete and FRP.

4. Cohesive zone modeling

In order to represent nonlinear fracture including interfacial debonding between concrete and FRP, the cohesive zone model is employed. In the cohesive zone model, the selection of a traction–separation relationship is one of essential aspects for the prediction of nonlinear fracture process [29]. For example, a linear softening model can overestimate FRP debonding behavior [14].
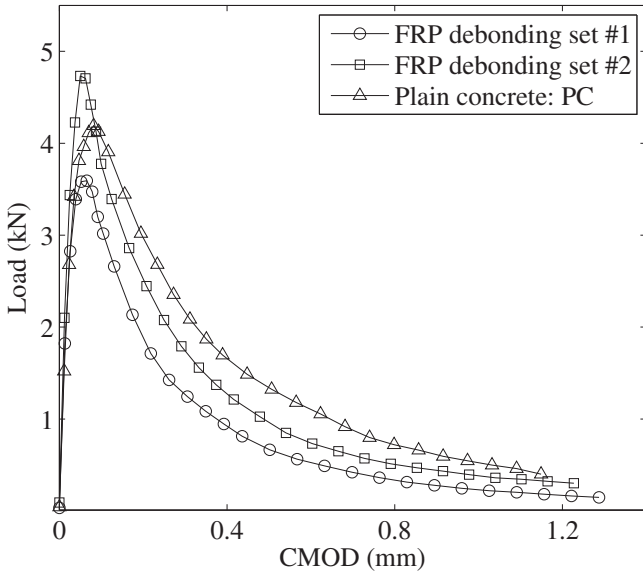
Table 3
Compressive strength test results and corresponding elastic modulus.

	Compressive strength (MPa)				Elastic modulus (GPa)
	Specimen #1	Specimen #2	Specimen #3	Average	
FRP debonding set 1	25.79	29.06	25.09	26.65	24.4
FRP debonding set 2	27.14	31.27	33.42	30.61	26.2
Plain concrete	24.01	23.53	26.95	24.83	23.6

Fig. 6. Averaged load-CMOD curves for each test set.

Then, in the following subsection, a traction-separation relation, which provides various initial descending slopes, is proposed with a single shape parameter for FRP debonding. Additionally, a bilinear softening model is briefly described for fracture of plain concrete.

4.1. Traction–separation relationship for FRP debonding

In order to provide various descending slopes in the cohesive zone model, a cohesive traction (T_n) versus separation (Δ_n) relationship with a shape parameter (α) is expressed as

$$T_n(\Delta_n) = \begin{cases} \dfrac{\sigma_{\max}}{\lambda \delta_n} \Delta_n & \text{for} \quad 0 \leq \Delta_n < \delta_{nc} \\ \dfrac{\sigma_{\max}}{1 - \lambda^\alpha}\left[1 - \left(\dfrac{\Delta_n}{\delta_n}\right)^\alpha\right] & \text{for} \quad \delta_{nc} \leq \Delta_n \leq \delta_n \\ 0 & \text{for} \quad \Delta_n > \delta_n \end{cases} \tag{2}$$

where λ and δ_n are an initial slope indicator and a complete separation, respectively. An initial slope indicator (λ) is defined as the ratio of a critical separation to a complete separation, i.e. $\lambda = \delta_{nc}/\delta_n$. The complete separation (δ_n) is the separation where the corresponding cohesive traction becomes zero, while the critical separation (δ_{nc}) is the separation where the corresponding cohesive traction is the cohesive strength (i.e. $T_n(\delta_{nc}) = \sigma_{\max}$). Note that the initial slope indicator is generally selected as a small value (e.g. 0.002 ~ 0.005) within the range of numerical stability in order to avoid large artificial compliance [37]. The complete separation is calculated by equating the fracture energy to the area under the traction-separation curve, which leads to

$$\delta_n = \frac{2G_F(1 - \lambda^\alpha)}{\sigma_{\max}}\left[1 - \lambda + \frac{\alpha - 1}{\alpha + 1}\left(1 - \lambda^{\alpha+1}\right)\right]^{-1} \tag{3}$$

When the cohesive separation (Δ_n) increases from zero to the critical separation, the proposed model demonstrates a simple linear traction–separation relationship. The smaller value of λ results in the higher initial ascending slope in the traction-separation relation. For the case of $\delta_{nc} \leq \Delta_n \leq \delta_n$, the traction-separation relation demonstrates nonlinear softening with a shape parameter (α). When separation is greater than the complete separation (δ_n), the cohesive traction is set to zero.

The effect of the shape parameter on the traction-separation relation is illustrated in Fig. 7. The fracture energy, the cohesive strength and the initial slope indicator are fixed as 150 N/m, 4 MPa and 0.001, respectively. The change of α results in the gradual change of the initial descending slope in the traction-separation relation. When the shape parameter is one, the model reproduces a linear softening model. While the shape parameter approaches zero, the initial descending slope becomes higher. For the comparison purpose, a power law cohesive zone model [43] is also plotted in Fig. 8 with the same fracture parameters. The traction-separation relation for the power law model is given as $T_n = \sigma_{\max}/(1 - \lambda)^\alpha(1 - \Delta_n/\delta_n)^\alpha$ when the cohesive separation is in between δ_{nc} and δ_n. If the shape parameter is greater than 7, it is difficult to distinguish for each traction-separation relation with regards to their shape. Thus, the proposed model provides more flexibility on the shape and initial descending slope than the previous power law cohesive zone model.
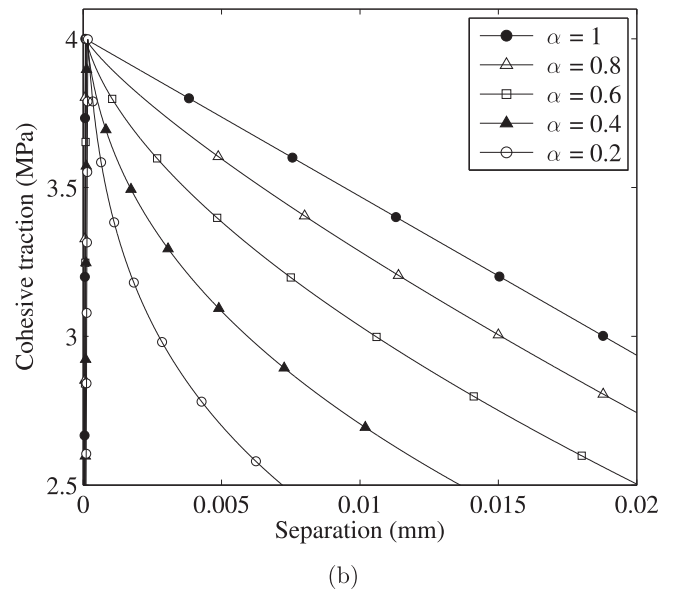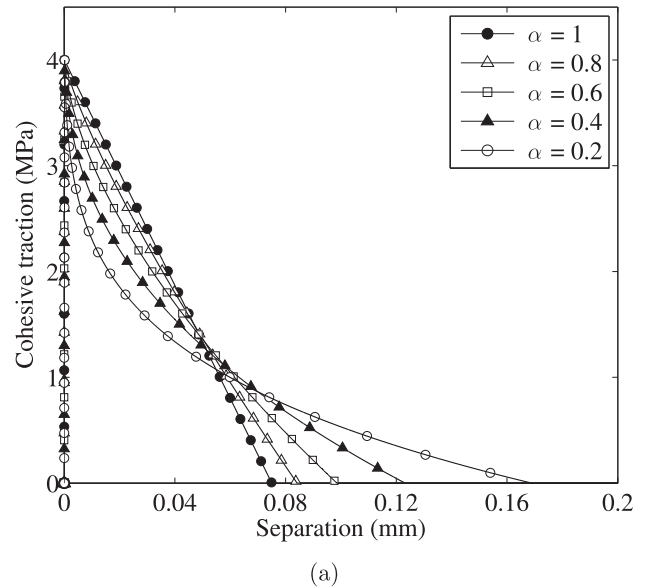

(a)

(b)

Fig. 7. Proposed traction–separation relationship: (a) effect of the shape parameter, and (b) zooming around the cohesive strength.

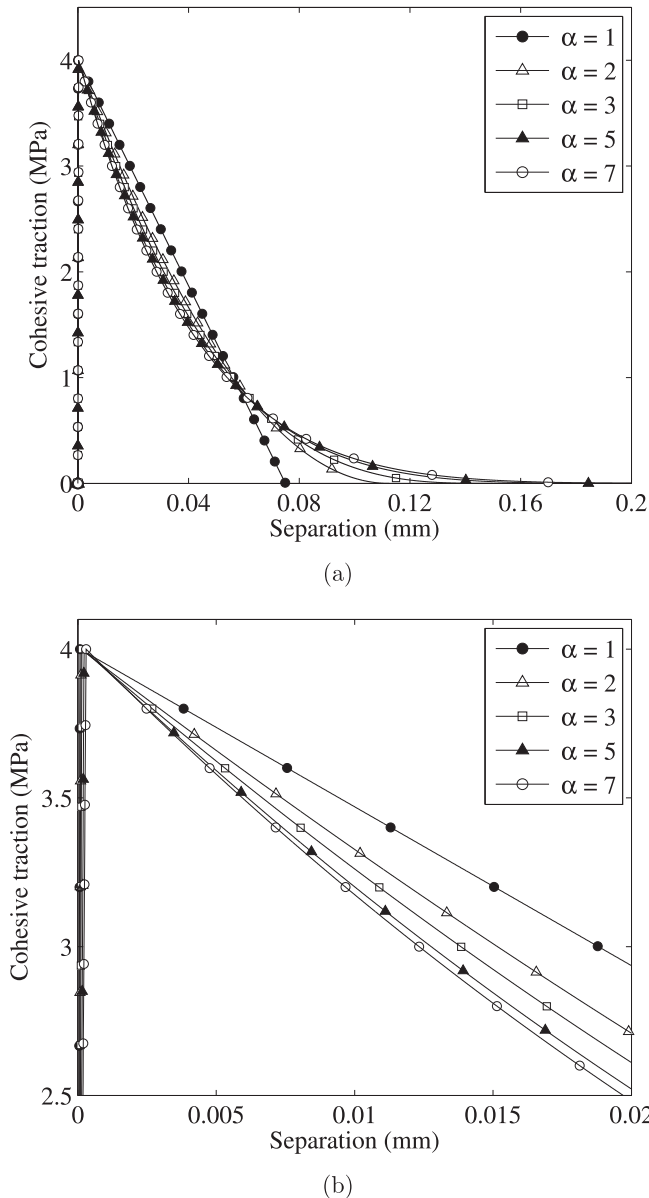Fig. 8. Traction–separation relationship by Song et al. [43]: (a) effect of the shape parameter, and (b) zooming around the cohesive strength.

4.2. Traction–separation relationship for plain concrete

For a traction–separation relationship of plain concrete, a bilinear softening model is generally utilized [6]. A bilinear softening model can be described by four parameters, i.e. the total fracture energy, the initial fracture energy, the cohesive strength, and the stress ratio of the kink point (see Fig. 9). The total fracture energy (G_F) is the total area under the traction-separation relation while the initial fracture energy (G_f) corresponds to the area under the initial descending line. The cohesive strength (σ_{max}) is the peak stress in the traction-separation relation, and the stress ratio of the kink point (ψ) is the ratio of the cohesive traction at the kink point to the cohesive strength. Based on the four fracture parameters of plain concrete, the horizontal axis intercept of the initial descending line is $\delta_1 = 2G_f/\sigma_{max}$, and the complete separation is given as
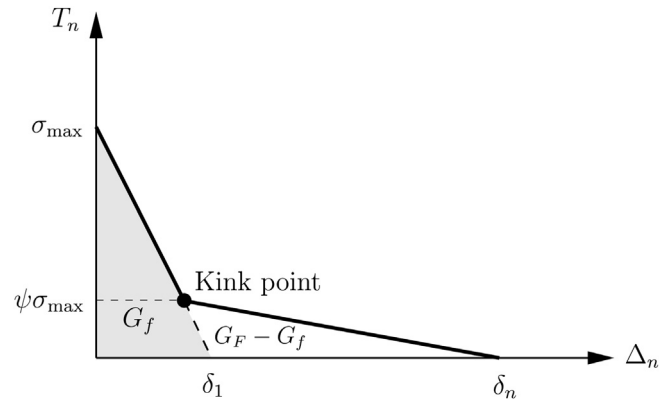

Fig. 9. Bilinear softening model for plain concrete.

$$\delta_n = \frac{2}{\psi\sigma_{max}}\left[G_F - (1-\psi)G_f\right] \qquad (4)$$

which is obtained from the relation between the total fracture energy and the area under the bilinear softening model.
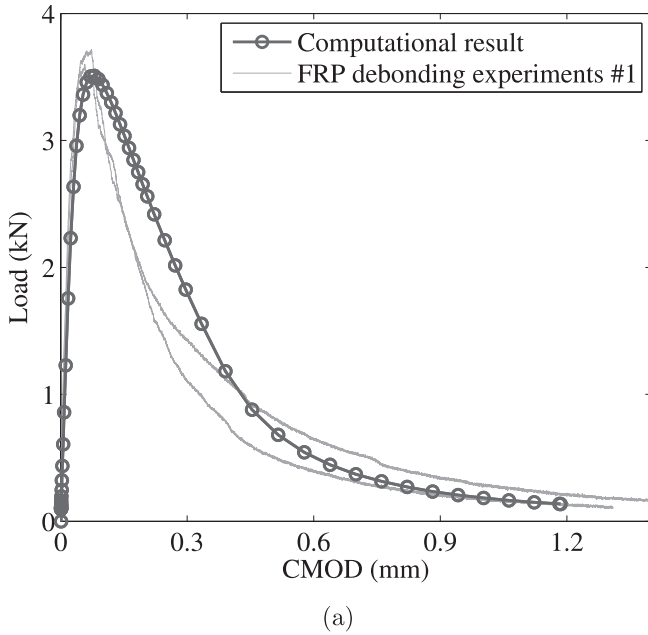
5. Computational results

Fracture behavior of the three-point bending test is simulated by utilizing the finite element analysis in conjunction with the cohesive zone model. The cohesive zone model is represented by employing the intrinsic cohesive surface element approach [49]. The intrinsic cohesive surface element is implemented through developing a user-defined element (UEL) subroutine in a commercial software, i.e. ABAQUS [1]. Finite element formulation and implementation procedures of the surface element are presented in-detail by Park and Paulino [28].

The geometry of the test configuration is illustrated in Fig. 2. The domain is discretized into bilinear quadrilateral elements and linear cohesive surface elements. Continuum behavior of plain concrete is represented by bilinear quadrilateral elements, while an FRP layer between two concrete blocks is not considered because the FRP layer does not provide significant effects on computational results in this study, as discussed later. The elastic modulus of plain concrete is obtained from Table 3, and the Poisson's ratio is selected as 0.25. Plain concrete fracture and interfacial debonding between concrete and FRP are characterized by utilizing cohesive surface elements. Cohesive elements are inserted along the potential crack path because the present study focuses on Mode-I fracture. The size of cohesive elements is selected as 1 mm, which is small enough to capture nonlinear fracture process zone in this study [37]. The cohesive strength and the total fracture energy are evaluated on the basis of the experiments for each test set, as shown in Tables 2 and 4.

For the FRP debonding computation, the proposed traction-separation relation (Eq. (2)) is utilized. The shape parameter (α) in the traction-separation relation is selected as 0.25, and the initial slope indicator is chosen as a small value within the numerical stability. Fig. 10 illustrates the good agreement between computational results and experimental results for the load-CMOD curves. For example, in the computational results, the peak load of the FRP-1 set (3.51 kN) is lower than the peak load of the FRP-2 set (4.18 kN), which corresponds to the experimental results.

For the prediction of plain concrete fracture behavior, the bilinear softening model is utilized. Because of the limited experimental data, the initial fracture energy and the stress ratio of the

(a)
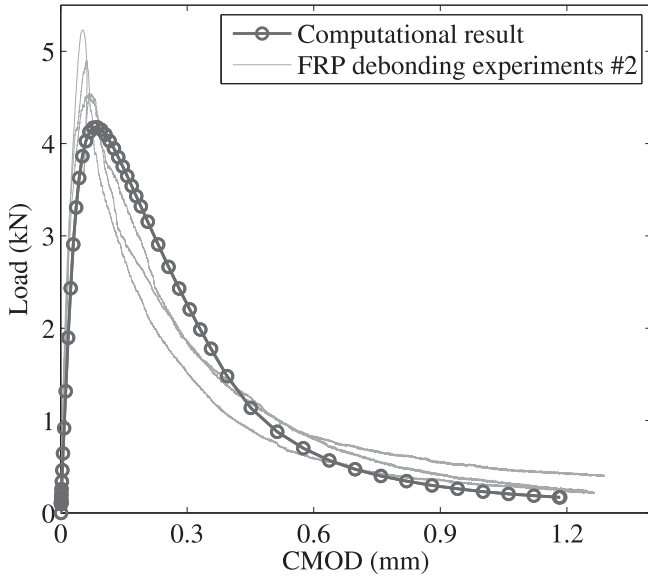
(b)

Fig. 10. Comparison between computational results and experiments for (a) the FRP-1 set and (b) the FRP-2 set.

kink point is assumed on the basis of previous works. Note that the ratio of the total fracture energy to the initial fracture energy (G_F/G_f) is generally within the range of 2.0 ~ 2.5 [5] and that the ratio of the kink point is between 0.15 and 0.33 [4]. In the present work, the initial fracture energy and the kink point ratio are selected as 126 N/m and 0.25, respectively. Alternatively, the bilinear softening model can be systematically determined in conjunction with the two-parameter fracture model [19,31]. Based on the evaluated material parameters and the assumptions, a load-CMOD curve of the computational result is plotted in Fig. 11, which agrees well with the experiments. In addition, the computational results also demonstrates that the peak load of the PC set (4.01 kN) is in between the peak load of the FRP-1 set and the peak load of the FRP-2 set, as observed in the experiments, although the evaluated tensile
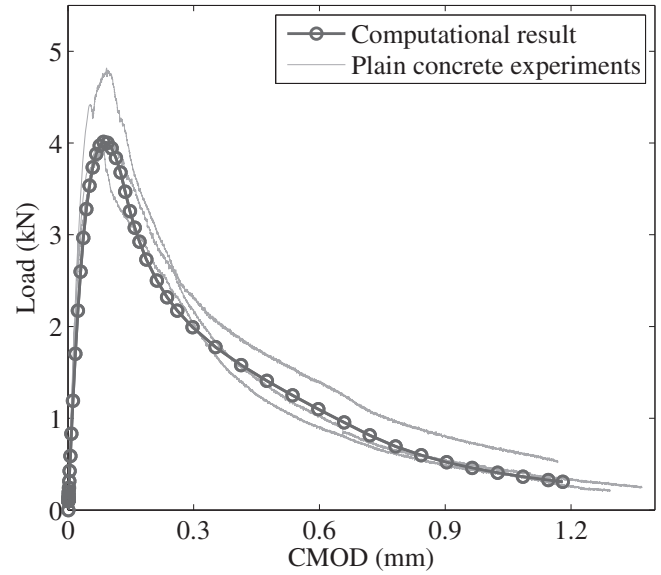

Fig. 11. Computational results of cohesive fracture for the plain concrete test.

strength of plain concrete is approximately 60 ~ 70% of the tensile strength of the FRP sets.

Additionally, the effect of an FRP layer on the computational results is investigated through introducing an FRP layer thickness of 2 mm in the finite element analysis. For the elastic modulus of the FRP layer, three values are selected as 250 GPa, 26.2 GPa and 2.5 GPa. Computational results for each case are plotted in Fig. 12. When the elastic modulus of the FRP layer is the same as the modulus of concrete (i.e. E_{FRP} = 26.2 GPa), its response is identical to the response without the FRP layer, as expected. When the elastic modulus of the FRP layer is selected as an actual material property, i.e. E_{FRP} = 250 GPa, although the difference is not significant, the peak load slightly increased from 4.18 kN to 4.23 kN because of the existence of a thin stiff layer. When the elastic modulus of the FRP layer is smaller than the modulus of concrete, the decrease of the peak load is observed. Then, the FRP layer, which is stiffer than plain concrete, can be eliminated for the computational simulation in this study.
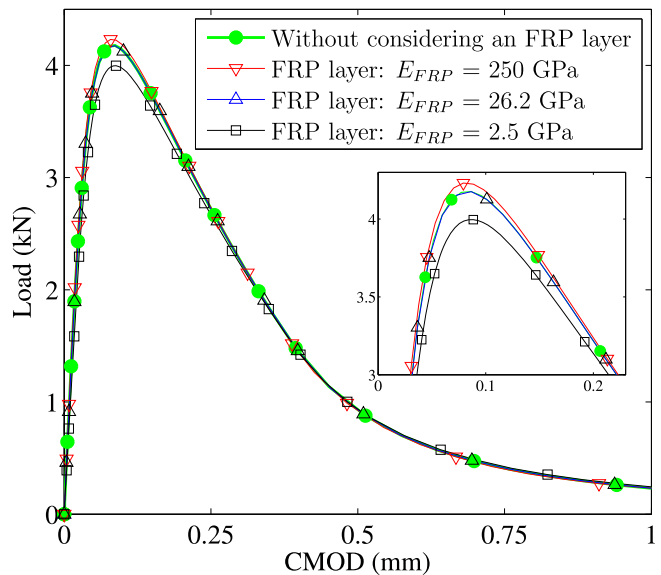

Fig. 12. Effect of an FRP layer on the computational results.

6. Conclusions

In order to investigate the mode-I interfacial fracture between concrete and FRP, experiments and computational simulation are integrated in conjunction with the cohesive zone model. For the estimation of the interfacial debonding characteristics, an experimental program is designed, which consists of three-point bending and splitting tests. Specimens are cut and bonded with an FRP sheet to measure the fracture energy and the cohesive strength of FRP debonding. Based on the evaluated fracture parameters, the interfacial fracture is predicted through creating a traction-separation relation, which provides various initial descending slopes. Computational results agree well with experimental results regarding load versus CMOD relations, which confirms the validity of the proposed experimental program and the measured fracture parameters. Additionally, experimental results illustrate that the FRP bonding strength is higher than the tensile strength of plain concrete. However, both experiments and computational results demonstrate that the peak load of FRP debonding can be lower than the peak load of plain concrete for the three-point bending tests because the fracture energy of FRP debonding can be significantly lower than the fracture energy of plain concrete. Therefore, both the fracture energy and the cohesive strength are essential fracture parameters to investigate the interfacial fracture behavior between concrete and FRP, and thus should be measured from fracture tests. Furthermore, mode-II and mixed-mode fracture tests and computations are also needed because delamination of an FRP layer generally occurs under mixed-mode failure conditions.

Acknowledgment

References

[1] Abaqus, Analysis User's Manual, Version 6.11, Dassault Systemes Simulia Corp., Providence, RI, USA, 2011.

[2] ACI Committee 440, Guide for the Design and Construction of Externally Bonded FRP Systems for Strengthening Concrete Structures, Tech. Rep. ACI Committee 440.2R-08, American Concrete Institute, 2008.

[3] G.I. Barenblatt, The formation of equilibrium cracks during brittle fracture: general ideas and hypotheses, axially symmetric cracks, Appl. Math. Mech. 23 (3) (1959) 622–636.

[4] Z.P. Bazant, Concrete fracture models: testing and practice, Eng. Fract. Mech. 69 (2) (2002) 165–205.

[5] Z.P. Bazant, E. Becq-Giraudon, Statistical prediction of fracture parameters of concrete and implications for choice of testing standard, Cem. Concr. Res. 32 (4) (2002) 529–556.

[6] Z.P. Bazant, J. Planas, Fracture and Size Effect in Concrete and Other Quasi-brittle Materials, CRC Press, Boca Raton, 1998.

[7] H.C. Biscaia, C. Chastre, M.A. Silva, Double shear tests to evaluate the bond strength between GFRP/concrete elements, Compos. Struct. 94 (2) (2012) 681–694.

[8] P.J. Burke, L.A. Bisby, M.F. Green, Effects of elevated temperature on near surface mounted and externally bonded FRP strengthening systems for concrete, Cem. Concr. Compos. 35 (1) (2013) 190–199.

[9] J.F. Chen, J.G. Teng, Anchorage strength models for FRP and steel plates bonded to concrete, J. Struct. Eng. 127 (7) (2001) 784–791.

[10] C.A. Coronado, M.M. Lopez, Sensitivity analysis of reinforced concrete beams strengthened with FRP laminates, Cem. Concr. Compos. 28 (1) (2006) 102–114.

[11] C.A. Coronado, M.M. Lopez, Numerical modeling of concrete-FRP debonding using a crack band approach, J. Compos. Constr. 14 (1) (2010) 11–21.

[12] D.S. Dugdale, Yielding of steel sheets containing slits, J. Mech. Phys. Solids 8 (2) (1960) 100–104.

[13] M. Elices, G.V. Guinea, J. Gomez, J. Planas, The cohesive zone model: advantages, limitations and challenges, Eng. Fract. Mech. 69 (2) (2002) 137–163.

[14] B. Ferracuti, M. Savoia, C. Mazzotti, Interface law for FRP concrete delamination, Compos. Struct. 80 (4) (2007) 523–531.

[15] fib Bulletin, Externally Bonded FRP Reinforcement for RC Structures, Tech. Rep. fib Bulletin No. 14, International Federation for Structural Concrete, 2001.

[16] A. Hillerborg, The theoretical basis of a method to determine the fracture energy G_F of concrete, Mater. Struct. 18 (4) (1985) 291–296.

[17] A. Hillerborg, M. Modeer, P.E. Petersson, Analysis of crack formation and crack growth in concrete by means of fracture mechanics and finite elements, Cem. Concr. Res. 6 (6) (1976) 773–781.

[18] L.C. Hollaway, A review of the present and future utilisation of FRP composites in the civil infrastructure with reference to their important in-service properties, Constr. Build. Mater. 24 (12) (2010) 2419–2445.

[19] Y.S. Jenq, S.P. Shah, Two parameter fracture model for concrete, J. Eng. Mech. – ASCE 111 (10) (1985) 1227–1241.

[20] A. Khalifa, W.J. Gold, A. Nanni, A.A. MI, Contribution of externally bonded FRP to shear capacity of rc flexural members, J. Compos. Constr. 2 (4) (1998) 195–202.

[21] Y.-R. Kim, D.H. Allen, D.N. Little, Damage-induced modeling of asphalt mixtures through computational micromechanics and cohesive zone fracture, J. Mater. Civ. Eng. 17 (5) (2005) 477–484.

[22] J.H. Lee, R.M. Chacko, M.M. Lopez, Use of mixed-mode fracture interfaces for the modeling of large-scale FRP-strengthened beams, J. Compos. Constr. – ASCE 14 (2010) 845–855.

[23] X.Z. Lu, J.G. Teng, L.P. Ye, J.J. Jiang, Bond-slip models for FRP sheets/plates bonded to concrete, Eng. Struct. 27 (6) (2005) 920–937.

[24] J. Lubliner, J. Oliver, S. Oller, E. Onate, A plastic-damage model for concrete, Int. J. Solids Struct. 25 (3) (1989) 299–326.

[25] C. Mazzotti, M. Savoia, B. Ferracuti, A new single-shear set-up for stable debonding of FRP-concrete joints, Constr. Build. Mater. 23 (4) (2009) 1529–1537.

[26] K. Nakaba, T. Kanakubo, T. Furuta, H. Yoshizawa, Bond behavior between fiber-reinforced polymer laminates and concrete, ACI Struct. J. 98 (3) (2001) 359–367.

[27] C.G. Papakonstantinou, P.N. Balaguru, Y. Auyeung, Influence of FRP confinement on bond behavior of corroded steel reinforcement, Cem. Concr. Compos. 33 (5) (2011) 611–621.

[28] K. Park, G.H. Paulino, Computational implementation of the PPR potential-based cohesive model in ABAQUS: educational perspective, Eng. Fract. Mech. 93 (2012) 239–262.

[29] K. Park, G.H. Paulino, Cohesive zone models: a critical review of traction-separation relationships across fracture surfaces, Appl. Mech. Rev. 64 (6) (2013), 060802–1–20.

[30] K. Park, G.H. Paulino, J. Roesler, Cohesive fracture model for functionally graded fiber reinforced concrete, Cem. Concr. Res. 40 (6) (2010) 956–965.

[31] K. Park, G.H. Paulino, J.R. Roesler, Determination of the kink point in the bilinear softening model for concrete, Eng. Fract. Mech. 75 (13) (2008) 3806–3818.

[32] N. Pesic, K. Pilakoutas, Concrete beams with externally bonded flexural FRP-reinforcement: analytical investigation of debonding failure, Compos. Part B Eng. 34 (4) (2003) 327–338.

[33] P.E. Petersson, Crack Growth and Development of Fracture Zones in Plain Concrete and Similar Materials, Tech. Rep. LUTVDG/TVBM-1006, Lund Institute of Technology, 1981.

[34] P. Qiao, Y. Chen, Cohesive fracture simulation and failure modes of FRP-concrete bonded interfaces, Theor. Appl. Fract. Mech. 49 (2) (2008) 213–225.

[35] P. Qiao, Y. Xu, Evaluation of fracture energy of composite-concrete bonded interfaces using three-point bend tests, J. Compos. Constr. 8 (4) (2004) 352–359.

[36] C. Rocco, G.V. Guinea, J. Planas, M. Elices, Review of the splitting-test standards from a fracture mechanics point of view, Cem. Concr. Res. 31 (1) (2001) 73–82.

[37] J. Roesler, G.H. Paulino, K. Park, C. Gaedicke, Concrete fracture prediction using bilinear softening, Cem. Concr. Compos. 29 (4) (2007) 300–312.

[38] W.M. Sebastian, Significance of midspan debonding failure in FRP-plated concrete beams, J. Struct. Eng. 127 (7) (2001) 792–798.

[39] A. Serbescu, M. Guadagnini, K. Pilakoutas, Standardised double-shear test for determining bond of FRP to concrete and corresponding model development, Compos. Part B Eng. 55 (2013) 277–297.

[40] S.T. Smith, J.G. Teng, FRP-strengthened RC beams. I: review of debonding strength models, Eng. Struct. 24 (4) (2002a) 385–395.

[41] S.T. Smith, J.G. Teng, FRP-strengthened RC beams. II: assessment of debonding strength models, Eng. Struct. 24 (4) (2002b) 397–417.

[42] S.H. Song, G.H. Paulino, W.G. Buttlar, Simulation of crack propagation in asphalt concrete using an intrinsic cohesive zone model, J. Eng. Mech. – ASCE 132 (11) (2006) 1215–1223.

[43] S.H. Song, M.P. Wagoner, G.H. Paulino, W.G. Buttlar, δ25 crack opening displacement parameter in cohesive zone models: experiments and simulations in asphalt concrete, Fatigue & Fract. Eng. Mater. Struct. 31 (10) (2008) 850–856.

[44] B. Taljsten, Defining anchor lengths of steel and CFRP plates bonded to concrete, Int. J. Adhes. Adhes. 17 (4) (1997) 319–327.

[45] J.G. Teng, J.F. Chen, S.T. Smith, L. Lam, FRP: Strengthened RC Structures, Wiley, New York, 2002.

[46] J.G. Teng, S.T. Smith, J. Yao, J.F. Chen, Intermediate crack-induced debonding in RC beams and slabs, Constr. Build. Mater. 17 (6–7) (2003) 447–462.

[47] R.S.Y. Wong, F.J. Vecchio, Towards modeling of reinforced concrete members with externally bonded fiber-reinforced polymer composites, ACI Struct. J. 100 (2003) 47–55.

[48] Z. Wu, J. Yin, Fracturing behaviors of FRP-strengthened concrete structures, Eng. Fract. Mech. 70 (10) (2003) 1339–1355.

[49] X.P. Xu, A. Needleman, Numerical simulations of fast crack growth in brittle solids, J. Mech. Phys. Solids 42 (9) (1994) 1397–1434.

[50] J. Yao, J.G. Teng, J.F. Chen, Experimental study on FRP-to-concrete bonded joints, Compos. Part B Eng. 36 (2) (2005) 99–113.